

## Difference analysis model for the mismatch effect and substrate-induced lattice deformation in atomically thin materials

Fang Wang (王芳),<sup>1</sup> B. Zhou (周斌),<sup>1</sup> Huimin Sun (孙惠敏),<sup>1</sup> Anyang Cui (崔安阳),<sup>1</sup> Ting Jiang (姜婷),<sup>1</sup> Liping Xu (徐丽萍),<sup>1</sup> Kai Jiang (姜凯),<sup>1</sup> Liyan Shang (商丽燕),<sup>1</sup> Zhigao Hu (胡志高),<sup>1,2,\*</sup> and Junhao Chu (褚君浩)<sup>1</sup>  
<sup>1</sup>Key Laboratory of Polar Materials and Devices (MOE) and Technical Center for Multifunctional Magneto-Optical Spectroscopy (Shanghai),  
 Department of Electronic Engineering, East China Normal University, Shanghai 200241, China  
<sup>2</sup>Collaborative Innovation Center of Extreme Optics, Shanxi University, Taiyuan, Shanxi 030006, China



(Received 12 April 2018; revised manuscript received 15 November 2018; published 5 December 2018)

Atomically thin materials hold mutative electronic transition properties by virtue of the inevitable strains adding to the lattice distribution. A quantitative approach and clear systematical verification have seldom been presented to effectively illustrate the substrate-induced strain along the lattice distribution, although the substrate perturbations for monolayers have been repeatedly mentioned. Here, a model of difference analysis is introduced to reveal the structural strain of monolayers from the substrate, which is derived from the mismatch effect based on the variation of the thermal expansion coefficient between the substrate and monolayers. A coupling coefficient is proposed to quantitatively manifest the substrate-induced strain and mismatch effect. Furthermore, combined with the coupling coefficient, the lattice disorder from the mismatch effect is demonstrated, experimentally using the WS<sub>2</sub> monolayer as reference. This study could promote broad investigations of some fundamental issues from preparation to electrical structural performances in atomically thin materials and further practical applications.

DOI: [10.1103/PhysRevB.98.245403](https://doi.org/10.1103/PhysRevB.98.245403)

### I. INTRODUCTION

Since the isolation of graphene as the first atomically thin two-dimensional (2D) material, the class of layered 2D materials with weak van der Waals interplanar bonding has expanded significantly [1–4]. Two-dimensional materials now span a great diversity of atomic structures and physical properties, which opens up the possibility for their application in transistors [5], electroluminescent devices [6], photodetectors [7], integrated circuits [8], and valleytronic and spintronic devices [9]. The prominent materials among these are the metalloids (graphene and black phosphorus), semiconductor chalcogenides of transition and basic metals (Mo, W, Ga, In, Sn, Re, etc.), and layered allotropes of other *p*-block elements of the periodic table such as P, As, Te, and so on [10–13]. On the other hand, owing to the atomically thin monolayer structure, the lattice distribution can be easily affected by external factors, such as the substrate type, the material-substrate bonding (even for the same substrate), the synthesis temperature, the charge doping of the substrate, the dielectric environment, the grain boundaries, the thermal conductivity coefficients, and thermal expansion coefficients of the substrate [14–18]. In most, if not all, real applications, atomically thin 2D materials are fabricated on a substrates or over a trench held at the edges. It results in the instability of the photoelectric properties. The pure effect of temperature variation on optical and electronic properties cannot be measured directly and compared with the calculations, which usually assume a freestanding monolayer. For example, the

measured luminescent transition of the WS<sub>2</sub> monolayer is varied from 1.88 to 2.01 eV, even when supported by the same substrate [14,19–21]. Some relations between the optical properties measured by photoluminescence (PL) or Raman spectroscopy within the mesoscale and the substrate-induced strain effects on the nanoscale have been repeatedly considered [14,15,22,23]. However, a quantitative approach and clear systematical verification have seldom been presented to describe the structure strain by substrate on the lattice distribution up to now. This study is vitally important for the fundamental understanding and application of 2D materials that are expected to be supported by a substrate in most circumstances.

Here, a widely practical WS<sub>2</sub> monolayer is considered as the model sample, which possesses obvious disturbed properties from the substrate-induced lattice deformation in atomically thin materials. We quantify the model of difference analysis by the parameter of the coupling coefficient  $\beta$ , which directly reveals the substrate-induced strain during the mismatch effect induced by the difference of the thermal expansion coefficient (TEC) in the monolayer-substrate system. With the slippage or realignment of monolayers on the substrate from the mismatch effect, different defect-bound exciton emission situations are brought to light with the help of PL analysis.

### II. METHODS

#### A. Synthesis of WS<sub>2</sub> monolayers

The WS<sub>2</sub> monolayers in this study were grown in the same environment by the low-pressure chemical vapor deposition

\*zghu@ee.ecnu.edu.cn

technique for 10 min. The 285-nm SiO<sub>2</sub>/Si substrates were cleaned using piranha solution (a volumetric mixture of 3:1 of 98% H<sub>2</sub>SO<sub>4</sub> to 35% H<sub>2</sub>O<sub>2</sub>), then placed face down on an alumina boat which contained WO<sub>3</sub> powder. The alumina boat was placed inside the quartz tube in the second zone. The temperature of the second zone was raised to 800 °C with a heating ramp of 10 °C min<sup>-1</sup>, and the deposition took place at 800 °C for 10 min. At the same time, the temperature of the first zone was also raised 200 °C to evaporate the sulfur powder. After the deposition, the furnace was allowed to cool naturally to room temperature. During the entire growth process, the argon flow rate was maintained at 80 sccm. The good crystallinity and thickness of the monolayers are confirmed by the Raman mapping and atomic force microscope (AFM) topographies.

### B. Optical and electronic characterizations

Temperature-dependent Raman/PL experiments were carried out by a Jobin-Yvon LabRAM HR Evolution spectrometer and a THMSE 600 heating/cooling stage (Linkam Scientific Instruments) in the temperature range from liquid-nitrogen temperature of -196 °C to 77 °C with a resolution of 0.1 °C. The WS<sub>2</sub> monolayers were excited by the 532-nm line of a solid-state laser and recorded in backscattering geometry with a resolution of better than 1 cm<sup>-1</sup>. The laser beam was focused through a 50× magnification microscope with a working distance of 18 mm. The output power of the 532-nm laser is controlled to be 13.9 μW, which remains unchanged during the whole experimental process. An air-cooled CCD (-70 °C) with a 1024×256 pixel front-illuminated chip was used to collect the scattered signal dispersed on 1800 grooves/mm grating for Raman and 300 grooves/mm grating for PL.

The topographies and surface potential distributions were investigated via an AFM (Dimension Icon, Bruker) with Pt/Ir-coated cantilevers in noncontact mode. An ac tip bias (2 kHz, 2000 mV) was applied here. Kelvin probe force microscopy (KPFM) was used to quantitatively characterize the discrepant contact potential difference (CPD) distribution. We used Pt/Ir-coated cantilevers in the noncontact mode so that the topography and surface potential signal could be measured simultaneously with a mechanical drive frequency of 68.3 kHz and an ac modulation of 2 V at 2 kHz. Tip bias was adjusted to cancel out the capacitive force generated by the work function disparity of  $\phi_{\text{tip}} - \phi_{\text{sample}}$  using the equation  $\text{CPD} \times e = \phi_{\text{tip}} - \phi_{\text{sample}}$  [24]. Here,  $\phi_{\text{tip}}$  and  $\phi_{\text{sample}}$  are the work functions of the tip and sample, respectively. The  $\phi_{\text{tip}}$  can be easily obtained if  $\phi_{\text{sample}}$  for the gold film is assumed to be 5.4 eV. The work function of the probe is always calibrated in advance by scanning a gold plate, and the corresponding CPD resolution is -0.6 mV. Accordingly, the work function for the probe  $\phi_{\text{tip}}$  is calibrated to be 4.8 eV. With the foregone  $\phi_{\text{tip}}$ , the information about the work function for samples can be derived by estimating the CPD distribution.

### C. Computational details

The Raman phonon eigensolutions were computed using the *ab initio* density functional theory (DFT) with a plane-wave pseudopotential method implemented in Ref. [25]. The

electron exchange correlation functional was treated using the generalized gradient approximation in the form proposed by Perdew, Burke, and Ernzerhof pseudopotentials [26]. The energy precision was set to 10<sup>-6</sup> eV, and atomic position was fully relaxed until the maximum force on each atom was less than 10<sup>-4</sup> eV/Å. A 600 eV energy cutoff was adopted, and the Brillouin zone was sampled with an 11×11×1  $\Gamma$ -centered Monkhorst-Pack *K*-point grid for geometry optimization and self-consistent calculations [27,28]. Equilibrium lattice constants  $a(T)$  at different temperatures were calculated by minimization of the Helmholtz free energy  $F(a, T)$  using the quasiharmonic approximation-based PHONOPY-QHA script [29,30]. For the minimization process,  $F(\{a_i\}, T)$  is obtained by fitting the discrete data points of  $F(\{a_i\}, T)$  to the third-order Birch-Murnaghan equation of state, where  $i$  is the label for different lattice constants or, equivalently, different strains.  $F(\{a_i\}, T)$  is constructed from  $\omega_{q,j}^i$  and  $E[a_i]$  through the following formula:  $F(\{a_i\}, T) = E[a_i] + \sum_{q,j} \frac{\hbar\omega_{q,j}^i}{2} + k_B T \sum_{q,j} \ln\{1 - \exp[-\frac{\hbar\omega_{q,j}^i}{k_B T}]\}$  [29]. Here,  $E[a_i]$  is the DFT ground-state energy;  $\omega_{q,j}^i$  is the phonon frequency at the  $q$  point with band index  $j$ . The sums run over all wave vectors and all bands of the whole Brillouin zone. The thermal expansion coefficients  $\alpha(T)$  for WS<sub>2</sub> and SiO<sub>2</sub> are then calculated through the following formula:  $\alpha(T) = da(T)/[a(T)dT]$ , where  $a(T)$  is the equilibrium lattice parameter corresponding to the minimum of the Helmholtz free energy [29]. The phonon interaction and spin-orbital coupling were not included in all calculations.

## III. THE EXPERIMENTAL FINDING OF RESIDUAL DEFORMATION

In most, if not all, atomically thin 2D materials, the synthetic process is conducted above room temperature. When synthetic samples return to room temperature, an unavoidable lattice deformation is residual in the monolayers because of the significant traction or contraction strain by substrate. The structural strain, proportional to the coupling coefficient, is derived from the mismatch effect induced by the TEC difference between the substrate and monolayers. The residual deformation is verified and analyzed by experimental characterizing and computational simulating WS<sub>2</sub> monolayers with different coupling features. The four model samples are called samples A, B, C, and D [Figs. 1(a)–1(d)].

Their PL peaks in Figs. 1(e)–1(h) are split into the neutral exciton (higher-energy  $A^0$ ) and charged exciton or trion (lower-energy  $A^-$ ), which originate from the transitions at the *K* point in the Brillouin zone [20,31,32]. There is a switch between  $A^0$  and the trion ( $A^-$  or  $A^+$  depending on the extra carrier type) at different Fermi levels [33–35]. Notably, the PL spectrum of sample D in Fig. 1(h) has to be fitted with three oscillator peaks. Moreover, the integral intensity decreases almost one order of magnitude compared with other monolayers. Considering the large linewidth of the extra peak (expressed as  $L$ ) and the dramatic decline of the PL intensity, we attributed peak  $L$  to the lattice distortion or disorder during the cooling process after synthesis at high temperature. The obvious emergence of defect trapping  $k_{\text{defect}}$

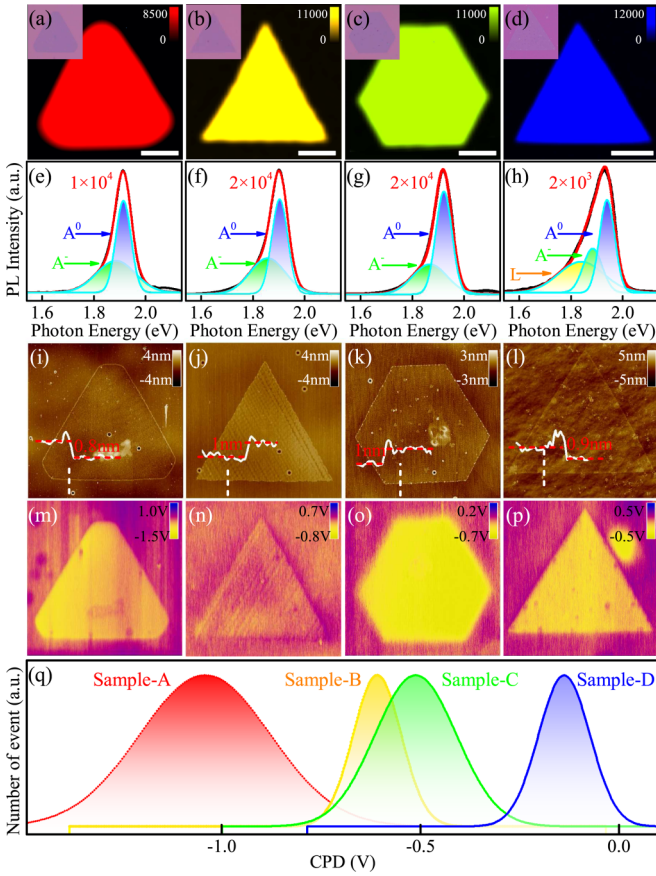


FIG. 1. (a)–(d) Raman mappings of the four monolayer samples. The insets show optical images from the corresponding mapping regions. The color bars correspond to the intensity of Raman spectra. (e)–(h) The PL spectra and multiple-peak fittings of the four monolayers. The intensity magnitudes of PL are displayed at the top. (i)–(l) The AFM topographies, confirming the monolayer nature of the samples. (m)–(p) The surface potential distributions of the four monolayers. (q) The Gaussian distribution of CPD for every sample. The scale bars of (a), (b), (c), and (d) are 9, 7, 9, and 13  $\mu\text{m}$ , respectively.

is an inducement of the reduction of luminescence quantum efficiency  $\eta_{\text{lum}} \approx k_{\text{rad}}/(k_{\text{rad}} + k_{\text{relax}} + k_{\text{defect}})$  in transition metal dichalcogenides [19,36].

The discrepant CPD distributions for samples A–D are further recorded with KPFM, which is widely employed to probe the local variations in the work functions of various surfaces [37]. Figures 1(i)–1(p) depict the sample topographies and surface potential images with  $\phi_{\text{tip}} = 4.8$  eV. The CPD of every sample shown in Fig. 1(q) is Gaussian-like regardless of the small topographic artifacts that are presumed to be particles deposited during postgrowth procedures. The differences in CPD distribution illustrate the discrepant Fermi levels among the four samples [37]. It further suggests that the structure strain from substrate results in lattice deformation and affects the distribution of electronic occupancy in electron energy bands. The substrate-induced strain should be taken into consideration for a variety of applications in optics and optoelectronics. More direct and effective analyses are impending. Raman scattering is one of the powerful tools

for discussing structure deformation by analyzing the phonon frequencies with a physical model.

#### IV. LINEAR ANALYSIS MODEL OF RAMAN SCATTERING

Figure 2 shows the Raman shifts of samples with different strain behaviors. The  $E_{2g}^1$  and  $A_{1g}$  modes are extracted from the Lorentzian fittings (Fig. S1 in the Supplemental Material [38]), where the  $E_{2g}^1$  mode is attributed to the in-plane relative motion between the two sulfur atoms and the W atom, whereas the  $A_{1g}$  mode is related to the out-of-plane vibration of two sulfur atoms in opposite directions.  $E_{2g}^1$  and  $A_{1g}$  are preliminarily analyzed by the linear approximation  $\omega(T) = \omega_0 + \chi T$ , where  $\omega_0$  is the extrapolated peak position at 0 K and  $\chi$  is the first-order temperature coefficient [39,40]. The preliminary linear analysis for  $E_{2g}^1$  and  $A_{1g}$  modes is shown with red solid lines in Figs. 2(e)–2(l). The plot of the peak position for  $E_{2g}^1$  versus temperature gives the slope  $\chi$  of samples A–D, which varies from  $-0.00383$  to  $-0.0129$   $\text{cm}^{-1} \text{K}^{-1}$ . The value of  $\chi$  for  $A_{1g}$  varies from  $-0.00458$  to  $-0.01222$   $\text{cm}^{-1} \text{K}^{-1}$ . The detailed fitting results are listed in Table S1 of the Supplemental Material [38]. Apparently, the absolute and relative magnitudes of the temperature coefficients  $\chi$  from four monolayers differ from each other significantly. The diversities, however, only prove the existence of different lattice deformations preliminarily. When the temperature changes, two effects are worth considering in the phonon vibration: the temperature dependence of the phonon frequencies and the modification of the phonon dispersion due to the substrate-induced strain. The parameters  $\chi$  from the linear analysis are related by both the effect of temperature and structure strain. Furthermore, the Raman frequency at low temperature is probably nonlinear or nonmonotonic. The small shifts of the phonon  $E_{2g}^1$  and  $A_{1g}$  around  $400$   $\text{cm}^{-1}$  also increase the fitting difficulty. As a result, it is impossible to clearly reveal the strain behavior with the parameter  $\chi$  from the primitive direct linear analysis. Therefore, we establish a model on the basis of the difference analysis to perfect the discussion of residual deformation and the strain effect in a monolayer-substrate system.

#### V. DIFFERENCE ANALYSIS MODEL

The model of difference analysis employs a data array consisting of phonon frequency, which is extracted from temperature-dependent Raman fittings and computational phonon frequencies. In detail, the frequency shift of intrinsic Raman spectra has been divided into thermal expansion of the lattice  $\Delta\omega_E$  and an anharmonic effect  $\Delta\omega_A$ . Thus, the Raman shift of freestanding atomically thin materials is given by [15]

$$\omega(T)_{\text{intrinsic}} = \omega_0 + \Delta\omega_E(T) + \Delta\omega_A(T), \quad (1)$$

where  $T$  is the measured temperature. The lattice constant of the sample structure increases due to thermal expansion, leading to the Raman shift, which is commonly expressed as  $\Delta\omega_E(T) = \omega_r \exp(-n\gamma \int_{300\text{K}}^T \alpha dT) - \omega_r$  [23]. Here,  $\omega_r$  is the intrinsic Raman frequency at room temperature,  $n$  is the degeneracy ( $n = 1$  for  $A_{1g}$  and  $n = 2$  for  $E_{2g}^1$ ),  $\gamma$  is the Grüneisen parameter, and  $\alpha$  is the thermal expansion coefficient of the material. The third term,  $\Delta\omega_A(T)$ ,

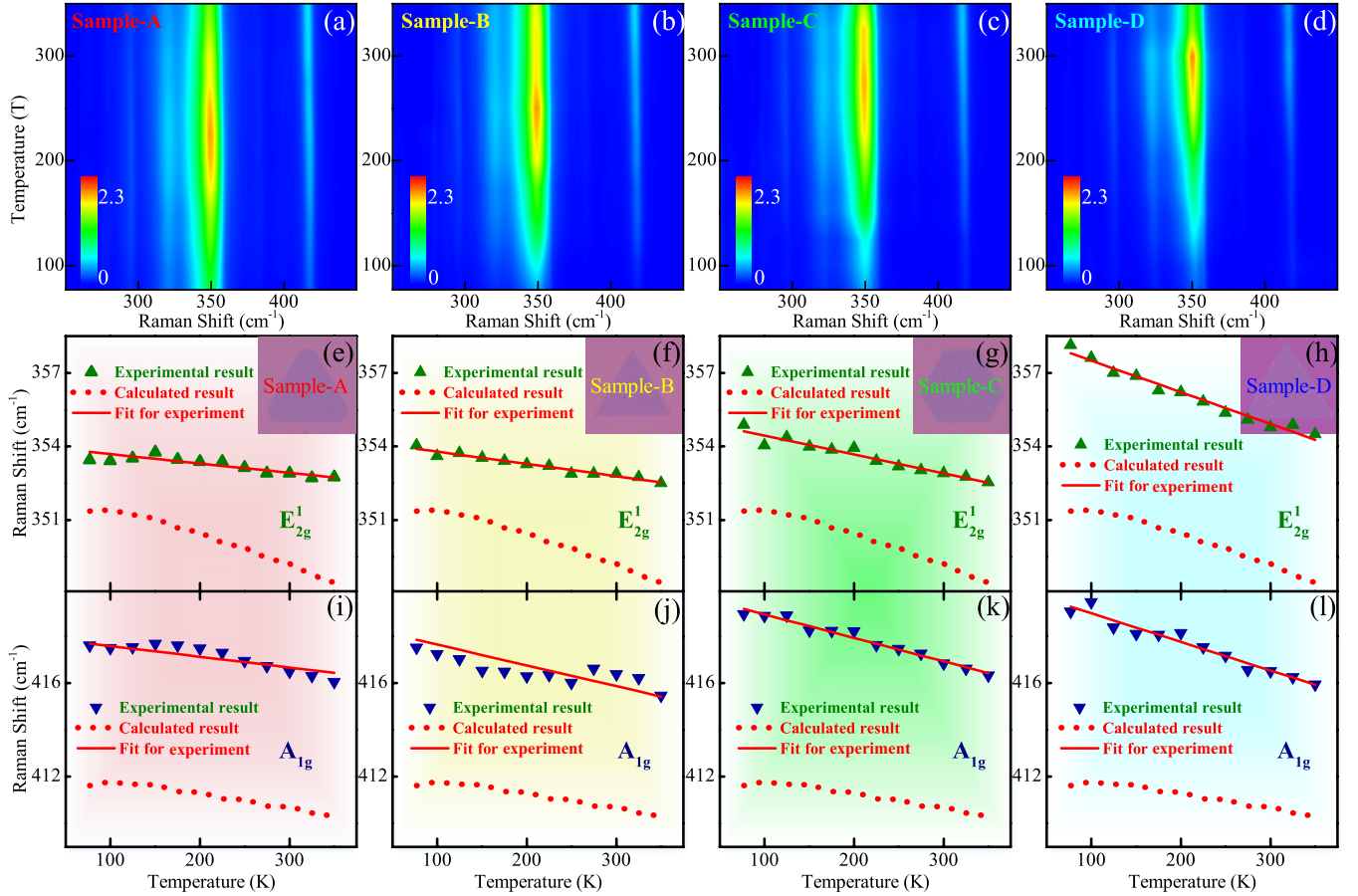


FIG. 2. Temperature-dependent Raman spectra of samples A–D. (a)–(d) Color contour mappings of Raman spectra (250–450 cm<sup>-1</sup>) as a function of temperature. The color bars correspond to the Raman intensity, which can be normalized to the Si peak. The Raman modes (e)–(h) for E<sub>2g</sub><sup>1</sup> and (i)–(l) A<sub>1g</sub><sup>1</sup> from temperature-dependent Raman shifts analyzed by experiment (triangles) and theoretical arithmetic (dots). The experimental results are preliminarily fitted with the linear model.

in Eq. (1) is determined by the optical phonon, which emerges accompanied by the absorption and emission of photons during the light-scattering process [41]. The optical phonon then decays via anharmonicity into two phonons and three phonons, which correspond to three- and four-phonon processes. The processes can be described by a semiquantitative simple model,  $\Delta\omega_A(T) = P_1[1 + \frac{2}{e^x - 1}] + P_2[1 + \frac{3}{e^y - 1} + \frac{3}{(e^y - 1)^2}]$ , where  $x = \hbar\omega/2k_B T$ ,  $y = \hbar\omega/3k_B T$  [41]. Here,  $\hbar$  is Planck's constant, and  $k_B$  is the Boltzmann constant. The first term corresponds to coupling of the optical phonon to two identical phonons, and the second term represents the coupling to three identical phonons. The coefficients  $P_1$  and  $P_2$  are constants that can be estimated by fitting the frequency shift attributed to anharmonic coupling. All fit parameters are extracted as  $\omega_r = 349.2$  cm<sup>-1</sup>,  $\gamma = 4.33$ ,  $P_1 = -0.902$ , and  $P_2 \approx 0$ .

As mentioned above,  $\omega_0$ ,  $\omega_r$ ,  $\Delta\omega_E$ , and  $\Delta\omega_A$  are the intrinsic temperature dependence characteristics of the freestanding monolayers. In the case of monolayers supported by the substrate, the residual deformation and the structural strain from the substrate have to be considered except for the usual thermal effects. Accordingly, the actual temperature-dependent frequency shifts of the Raman phonon for monolayers on the

substrate should be given as [15]

$$\omega(T)_{\text{experiment}} = \omega_0 + \Delta\omega_{RT} + \Delta\omega_E(T) + \Delta\omega_A(T) + \Delta\omega_M(T), \quad (2)$$

where  $\Delta\omega_{RT}$  is the result of the residual deformation, which is introduced by the mismatch effect when the high-temperature synthetic monolayers return to room temperature.  $\Delta\omega_M(T)$  is the effect of substrate-induced strain  $\beta\varepsilon(T)$  due to the TEC mismatch. It can be expressed as [15]

$$\begin{aligned} \Delta\omega_M(T) &= \beta\varepsilon(T) \\ &= \beta \int_{300\text{K}}^T [\alpha_{\text{WS}_2}(T) - \alpha_{\text{SiO}_2}(T)] dT, \end{aligned} \quad (3)$$

where  $\beta$  is the coupling coefficient, indicating the substrate coupling effect and  $\varepsilon(T)$  is the basic mismatch strain related to the temperature-dependent TECs of SiO<sub>2</sub> ( $\alpha_{\text{SiO}_2}$ ) and WS<sub>2</sub> ( $\alpha_{\text{WS}_2}$ ).

Using the description above, one can extract the Raman frequency shift related to only the residual deformation and substrate-induced strain in the temperature-changing process by subtracting the intrinsic temperature-dependent Raman shift from the experimental data. Here, the intrinsic Raman

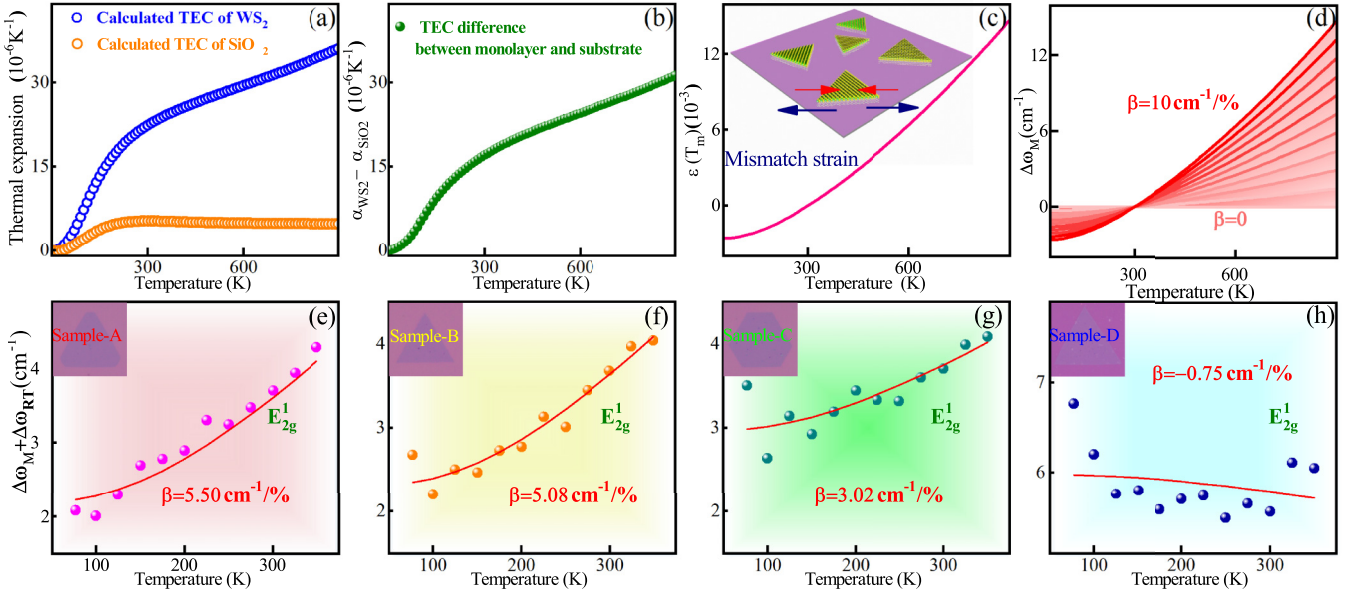


FIG. 3. (a) Calculated TEC of  $\text{SiO}_2$  and monolayer  $\text{WS}_2$ . (b) TEC difference between the monolayer and substrate ( $\alpha_{\text{WS}_2} - \alpha_{\text{SiO}_2}$ ). (c) The evolution of basic mismatch strain  $\varepsilon$  with temperature increasing from 77 to 900 K. The inset illustrates the schematic of the thermal contraction of monolayers on the substrate during the cooling process. (d) The effect of substrate-induced strain  $\Delta\omega_M(T)$  when the coupling coefficient  $\beta$  changes from 0 to  $10 \text{ cm}^{-1}/\%$ . (e)–(h)  $\Delta\omega_M(T) + \Delta\omega_{RT}$  [ $\Delta\omega_M(T)$  is the substrate-induced strain effect;  $\Delta\omega_{RT}$  is the residual strain effect] from frequency variations of Raman spectra for the  $E_{2g}^1$  mode in samples A, B, C, and D. The parameter  $\beta$  is the coupling coefficient, which indicates the substrate coupling strain.

spectra are extracted from the red dotted lines for the calculated results in Fig. 2, which refer to the theoretical shifts for a freestanding film:

$$\begin{aligned} \Delta\omega_{RT} + \Delta\omega_M(T) &= \omega(T)_{\text{experiment}} - \omega(T)_{\text{intrinsic}} \\ &= \Delta\omega_{RT} + \beta \int_{300\text{K}}^T [\alpha_{\text{WS}_2}(T) \\ &\quad - \alpha_{\text{SiO}_2}(T)] dT. \end{aligned} \quad (4)$$

The calculated TEC data for individual components of the system are plotted as a function of temperature in Fig. 3(a). Assuming that the monolayer is pinned on the substrate throughout the whole temperature range,  $\varepsilon(T)$  can be estimated as a function of temperature [Fig. 3(c)]. For a wider applicability of the difference analysis model,  $\varepsilon(T)$  is extended to 900 °C, which is beyond the experimental results in this work. The effect of substrate-induced strain  $\Delta\omega_M(T)$  for a monolayer with different bonding conditions on the substrate (coupling coefficient from  $\beta = 0$  to  $\beta = 10 \text{ cm}^{-1}/\%$ ) is shown in Fig. 3(d). It illustrates the different TEC mismatch effects of  $\Delta\omega_M(T)$  in the case when the monolayer is pinned on the substrate throughout the whole process and no slippage or realignment of monolayers on the surface of the substrate occurs. Here, the effect of residual deformation  $\Delta\omega_{RT}$  is the result of the cooling process after synthesis, which is likely to be accompanied by a series of complex phenomena, such as wrinkles, cracks, strain relaxation, and so on. It can be extracted from the fitting results in the following. The sums of  $[\Delta\omega_M(T) + \Delta\omega_{RT}]$  for samples A–D are obtained by subtracting the intrinsic temperature-dependent Raman shifts from the experimental data. Here, the intrinsic Raman

shift is extracted from the theoretical value (Fig. S2 in the Supplemental Material [38]). With  $\varepsilon(T)$  integrated from the calculated TECs of the substrate and monolayer, the sums of  $[\Delta\omega_M(T) + \Delta\omega_{RT}]$  are fitted in Figs. 3(e)–3(h).

The fitting parameters of  $\Delta\omega_{RT}$  and  $\beta$  are listed in Table I. The decline of the coupling coefficient indicates that the structure strain from the substrate coupling decreases from sample A to sample D. In addition, as shown in Figs. 3(g) and 3(h), the fitting curves for samples C and D cannot match the sum of  $[\Delta\omega_M(T) + \Delta\omega_{RT}]$  accurately, especially for sample D. The experimental value is higher than the fitting results at low temperature, which seems like a curled-up tail. The tail also appears in Fig. 3(f) for sample B slightly. It can be understood in the following way: when the coupling interaction between the monolayer and the substrate is not strong enough, it results in the slippage or realignment of monolayers on the surface of the substrate. In such cases, the substrate strain induced by the mismatch effect would not be coherent and would be less than in the coherently strained case. And wrinkles or cracks may arise during the process [42]. The deformation potential from the pronounced slippage or realignment is the

TABLE I. Fitting parameters of  $\Delta\omega_{RT}$  and  $\beta$  for  $E_{2g}^1$  from samples A–D.

Sample	$\Delta\omega_{RT}$ ( $\text{cm}^{-1}$ )	$\beta$ ( $\text{cm}^{-1}/\%$ )
A	3.61	5.50
B	3.63	5.08
C	3.75	3.02
D	5.79	−0.75

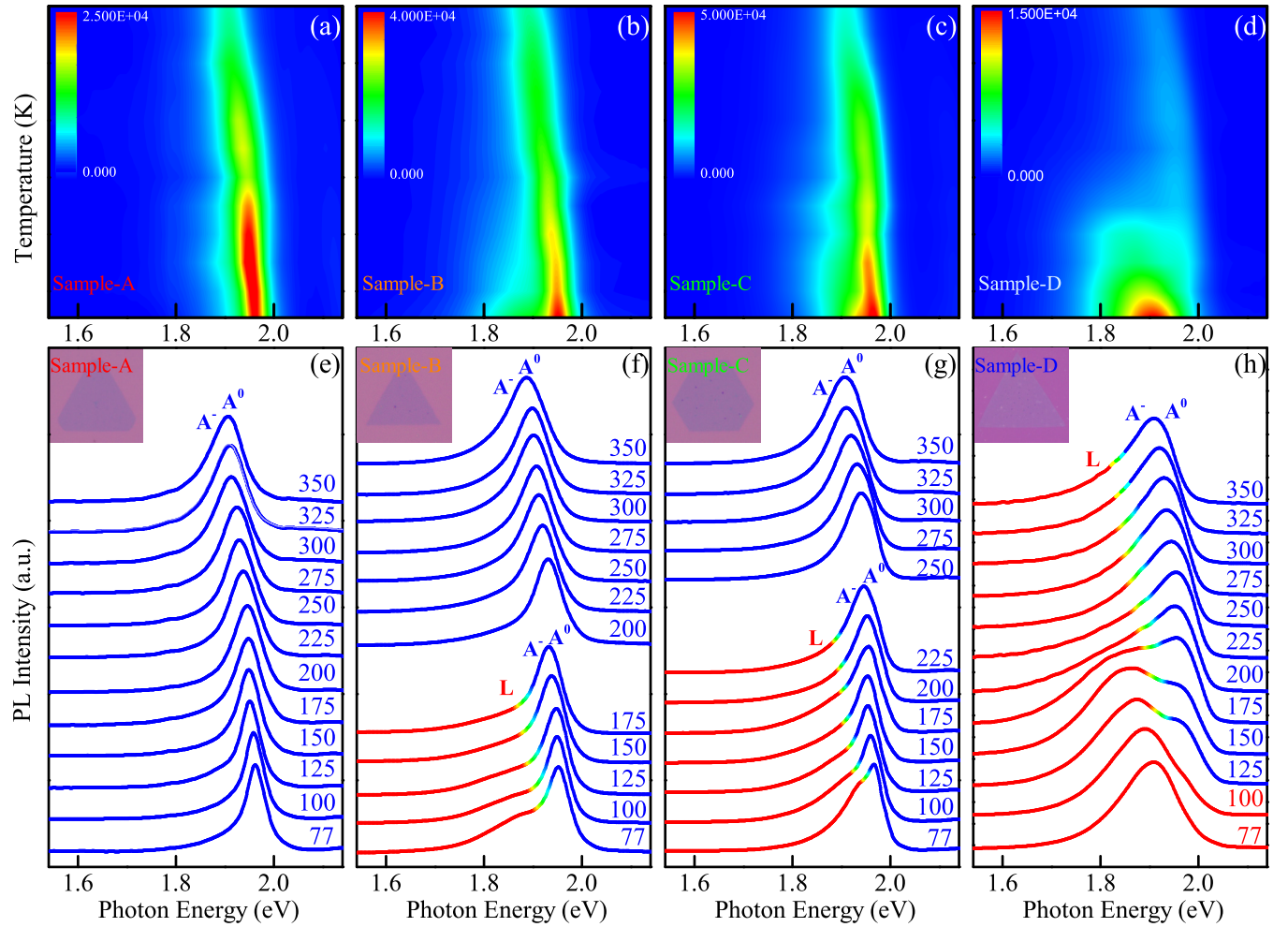


FIG. 4. Temperature-dependent PL spectra of four monolayers. (a)–(d) Color contour mappings of PL spectra (1.54–2.14 eV) as a function of temperature. The color bars correspond to the intensity of the PL spectra. (e)–(h) Normalized temperature-dependent PL spectra of samples A, B, C, and D, respectively.

cause of the negative value of  $\beta$  in sample D. However, the quantitative analysis of the deformation potential needs more rigorous research with complex models and microscopic analysis. Furthermore, the deformation potential also contributes to the nonmonotonic evolution of the Raman intensity with temperature (Fig. S3 in the Supplemental Material [38]), which is incompatible with the calculated Raman results in Fig. S2 in the Supplemental Material [38]. On the other hand, it is common for the calculated phonon frequency to be off by a few wave numbers compared to experimental data for very well studied semiconductor materials. As a result,  $\omega_r$  in the present study is about  $4 \text{ cm}^{-1}$  smaller than the approximate reference for a freestanding monolayer from the experimental measurement in a previous report [14]. With the development and optimization of the study for the intrinsic property of the freestanding monolayer, more accurate results could be presented with the difference analysis model. The finding is vitally important for the fundamental understanding of the interface effect and application of 2D materials that are expected to be supported by a substrate in most circumstances.

## VI. LATTICE DISORDER BY THE MISMATCH EFFECT

As discussed above, if the coupling interaction in the system of the monolayer and substrates is not strong enough, a slippage or realignment of monolayers on the surface of the substrate occurs easily during the temperature-changing process. It is an inducement for the wrinkles or rips in the monolayers, which promote the trapping of free mobile excitons by the surface impurities. For further exploration of the lattice disorder caused by the mismatch effect, temperature-dependent PL spectra are performed for samples A–D. Figures 4(a)–4(d) characterize the obvious redshift and apparent attenuation of PL intensities, which is attributed to the increasing nonradiative electron-hole recombination rate [43–46]. In addition to this conventional phenomenon, an extra peak at lower energy (labeled L) is observed in samples B–D from the normalized spectra in Figs. 4(e)–4(h). The large linewidth of peak L, especially for sample D with a linewidth more than 150 meV at 77 K, is an evident indication for the existence of small crystalline domains by lattice distortion. Interestingly, the crystal structure is more disordered for the

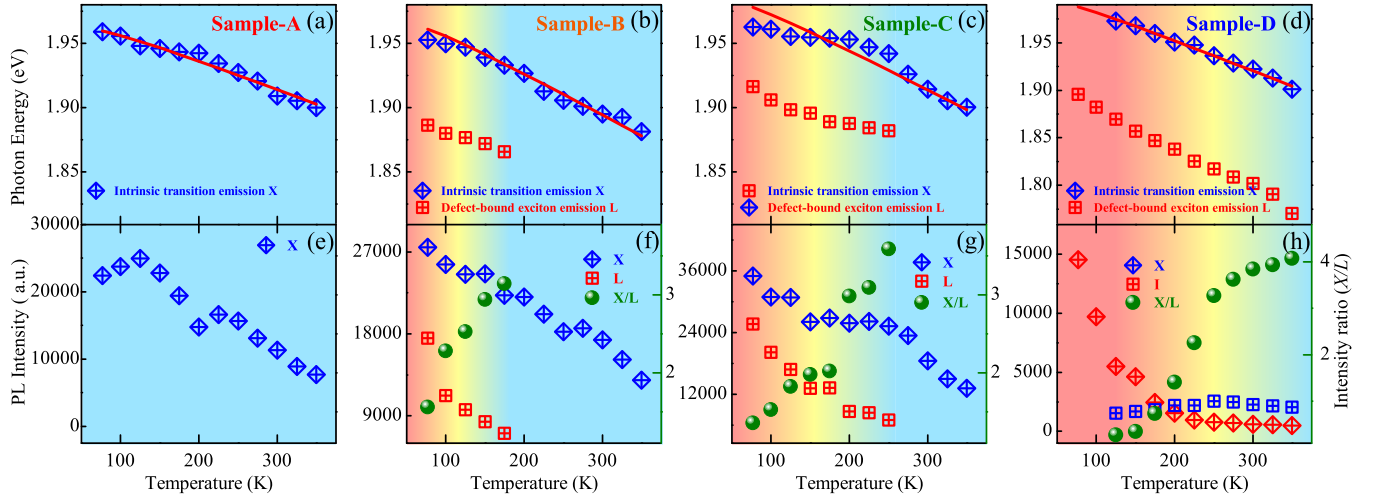


FIG. 5. Gaussian fitting results for monolayers. (a)–(d) Peak position of the intrinsic transition exciton  $X$  and defect-bound exciton emission  $L$  of samples A–D. (e)–(h) PL intensity of exciton  $X$  and  $L$  of samples A–D, respectively. The green dots in (f)–(h) show the intensity ratios of intrinsic to defect-bound excitons ( $X/L$ ).

sample with weaker coupling interaction with the substrate, which slips more during the temperature-changing process.

The detailed transition evolutions for samples A–D are distinct in the Gaussian fitting results (Fig. 5). For the purpose of gaining insight into the low-energy transitions from the lattice disorder in samples A–D, the transition exciton  $A^0$  and trion  $A^-$  are fitted with one peak,  $X$ . Evidently, peak  $L$  is more significant at low temperature. The thermal energy at low temperature is not enough to avoid the trapping of the free mobile excitons in defect sites, and hence, they can be localized/trapped and recombine radiatively to emit photons. However, by laterally comparing peak  $L$  of samples A–D at the same temperature, the lattice disorder caused by the slippage or realignment from different coupling interactions is still a significant and unavoidable factor for peak  $L$ . With the decrease in the substrate coupling strain from sample A to sample D, the restriction of the slippage or realignment of monolayers on the substrate becomes weaker. Accordingly, the exciton  $L$  at low temperature varies gradually from dull to remarkable as the lattice distortion is more and more significant from sample A to sample D. The defect-bound exciton of the slippage is especially obvious for sample D in Figs. 4(h) and 5(h), where the free-exciton emission of  $\text{WS}_2$  obviously quenches and totally disappears when the temperature is below 100 K. Except for samples A–D, more lattice distortion conditions in different coupling situations are brought shown in Fig. S4 in the Supplemental Material [38].

TABLE II. Fitting parameters of the PL peak energy as a function of temperature extracted in Figs. 5(a)–5(d).

Sample	$E_0$ (eV)	$\langle \hbar\omega \rangle$ (meV)	$S$
A	1.963	17.052	1.354
B	1.968	14.855	1.923
C	1.985	14.034	1.824
D	1.996	12.725	1.892

In addition, we fit the peak of intrinsic transition excitons under different situations of lattice distortion with a physical model. The redshifts with increasing temperature arise from the electron-phonon interactions and slight changes in bond lengths. By employing a modified Varshni relationship, the redshifts of the direct transitions with temperature can be fitted using [34,47]

$$E(T) = E_0 - S \langle \hbar\omega \rangle \left[ \coth \frac{\langle \hbar\omega \rangle}{2k_B T} - 1 \right], \quad (5)$$

where  $E_0$  is the emission energy at 0 K,  $S$  is the Huang-Rhys factor that represents the coupling strength of the exciton and phonon, and  $\langle \hbar\omega \rangle$  is the average phonon energy. The fitting parameters are given in Table II, which lists the fitting values of  $E_0$ ,  $S$ , and  $\langle \hbar\omega \rangle$  for samples A–D. The finding is significantly meaningful in estimating the properties of practical applications based on 2D materials.

Importantly, our analysis model could also be applied to other monolayer systems with wide characterizations of Raman and PL spectra. The exploration promotes the effective analysis of crystallinity and optimization of the preparation conditions with coupling confidence for single-layer 2D material systems.

## VII. CONCLUSIONS

To summarize, a difference analysis model was introduced in the temperature-dependent Raman scattering to describe the substrate strain, which is in the mismatch effect by the TEC difference between the substrate and atomically thin materials. The coupling coefficient was extracted from the analysis model. It expresses the substrate-induced strain and mismatch effect effectively. The conclusion was further adopted in the analysis of a defect-bound exciton by the slippage or realignment of monolayers on the substrate during the mismatch effect. This reliable approach of difference analysis can be broadly applied to the study of the strain-based interface effect in 2D materials in functional systems such as ferroelectric and flexible substances.

## ACKNOWLEDGMENTS

One of the authors (F.W.) would like to thank Prof. S. Gong for the constructive discussions. This work was financially supported by the National Key Research and Development Program of China (Grant No. 2017YFA0303403), the Natural Science Foundation of China (Grants No. 61674057 and No.

61227902), Projects of Science and Technology Commission of Shanghai Municipality (Grants No. 18JC1412400, No. 18YF1407200, No. 18YF1407000, and No. 15JC1401600), and the Program for Professor of Special Appointment (Eastern Scholar) at Shanghai Institutions of Higher Learning and the Fundamental Research Funds for the Central Universities.

- [1] S. Wu, S. Buckley, J. R. Schaibley, L. Feng, J. Yan, D. G. Mandrus, F. Hatami, W. Yao, J. Vučković, A. Majumdar, and X. Xu, *Nature (London)* **520**, 69 (2015).
- [2] D. Kozawa, R. Kumar, A. Carvalho, K. Kumar Amara, W. Zhao, S. Wang, M. Toh, R. M. Ribeiro, A. H. Castro Neto, K. Matsuda, and G. Eda, *Nat. Commun.* **5**, 4543 (2014).
- [3] B. C. Marin, S. E. Root, A. D. Urbina, E. Aklile, R. Miller, A. V. Zaretski, and D. J. Lipomi, *ACS Omega* **2**, 626 (2017).
- [4] T. Georgiou, R. Jalil, B. D. Belle, L. Britnell, R. V. Gorbachev, S. V. Morozov, Y.-J. Kim, A. Gholinia, S. J. Haigh, O. Makarovskiy, L. Eaves, L. A. Ponomarenko, A. K. Geim, K. S. Novoselov, and A. Mishchenko, *Nat. Nanotechnol.* **8**, 100 (2013).
- [5] Y.-H. Lee, L. Yu, H. Wang, W. Fang, X. Ling, Y. Shi, C.-T. Lin, J.-K. Huang, M.-T. Chang, C.-S. Chang, M. Dresselhaus, T. Palacios, L.-J. Li, and J. Kong, *Nano Lett.* **13**, 1852 (2013).
- [6] R. S. Sundaram, M. Engel, A. Lombardo, R. Krupke, A. C. Ferrari, P. Avouris, and M. Steiner, *Nano Lett.* **13**, 1416 (2013).
- [7] Z. Yin, H. Li, H. Li, L. Jiang, Y. Shi, Y. Sun, G. Lu, Q. Zhang, X. Chen, and H. Zhang, *ACS Nano* **6**, 74 (2012).
- [8] B. Radisavljevic, M. B. Whitwick, and A. Kis, *ACS Nano* **5**, 9934 (2011).
- [9] H. Zeng, J. Dai, W. Yao, D. Xiao, and X. Cui, *Nat. Nanotechnol.* **7**, 490 (2012).
- [10] K. F. Mak, C. Lee, J. Hone, J. Shan, and T. F. Heinz, *Phys. Rev. Lett.* **105**, 136805 (2010).
- [11] Q. H. Wang, K. Kalantar-Zadeh, A. Kis, J. N. Coleman, and M. S. Strano, *Nat. Nanotechnol.* **7**, 699 (2012).
- [12] D. Jariwala, V. K. Sangwan, L. J. Lauhon, T. J. Marks, and M. C. Hersam, *ACS Nano* **8**, 1102 (2014).
- [13] A. J. Mannix, B. Kiraly, M. C. Hersam, and N. P. Guisinger, *Nat. Rev. Chem.* **1**, 0014 (2017).
- [14] L. Su, Y. Yu, L. Cao, and Y. Zhang, *Nano Res.* **8**, 2686 (2015).
- [15] D. Yoon, Y.-W. Son, and H. Cheong, *Nano Lett.* **11**, 3227 (2011).
- [16] Y. Wan, H. Zhang, K. Zhang, Y. Wang, B. Sheng, X. Wang, and L. Dai, *ACS Appl. Mater. Interfaces* **8**, 18570 (2016).
- [17] A. M. van der Zande, P. Y. Huang, D. A. Chenet, T. C. Berkelbach, Y. You, G.-H. Lee, T. F. Heinz, D. R. Reichman, D. A. Muller, and J. C. Hone, *Nat. Mater.* **12**, 554 (2013).
- [18] S. Tongay, J. Zhou, C. Ataca, K. Lo, T. S. Matthews, J. Li, J. C. Grossman, and J. Wu, *Nano Lett.* **12**, 5576 (2012).
- [19] F. Wang, J. Y. Wang, S. Guo, J. Z. Zhang, Z. G. Hu, and J. H. Chu, *Sci. Rep.* **7**, 44712 (2017).
- [20] Y. Wang, C. Cong, W. Yang, J. Shang, N. Peimyoo, Y. Chen, J. Kang, J. Wang, W. Huang, and T. Yu, *Nano Res.* **8**, 2562 (2015).
- [21] A. P. S. Gaur, S. Sahoo, J. F. Scott, and R. S. Katiyar, *J. Phys. Chem. C* **119**, 5146 (2015).
- [22] B. G. Shin, G. H. Han, S. J. Yun, H. M. Oh, J. J. Bae, Y. J. Song, C.-Y. Park, and Y. H. Lee, *Adv. Mater.* **28**, 9378 (2016).
- [23] L. Su, Y. Zhang, Y. Yu, and L. Cao, *Nanoscale* **6**, 4920 (2014).
- [24] J. H. Kim, J. Lee, J. H. Kim, C. C. Hwang, C. Lee, and J. Y. Park, *Appl. Phys. Lett.* **106**, 251606 (2015).
- [25] C. Trallero-Giner, K. Kunc, and K. Syassen, *Phys. Rev. B* **73**, 205202 (2006).
- [26] P. Giannozzi, S. Baroni, N. Bonini, M. Calandra, R. Car, C. Cavazzon, D. Ceresoli, G. L. Chiarotti, M. Cococcioni, I. Dabo, A. D. Corso, S. de Gironcoli, S. Fabris, G. Fratesi, R. Gebauer, U. Gerstmann, C. Gougoussis, A. Kokalj, M. Lazzeri, L. Martin-Samos, N. Marzari, F. Mauri, R. Mazzarello, S. Paolini, A. Pasquarello, L. Paulatto, C. Sbraccia, S. Scandolo, G. Sclauzero, A. P. Seitsonen, A. Smogunov, P. Umari, and R. M. Wentzcovitch, *J. Phys.: Condens. Matter* **21**, 395502 (2009); code available from <http://www.quantum-espresso.org>.
- [27] H. J. Monkhorst and J. D. Pack, *Phys. Rev. B* **13**, 5188 (1976).
- [28] G. P. Srivastava and I. O. Thomas, *Phys. Rev. B* **98**, 035430 (2018).
- [29] N. Mounet and N. Marzari, *Phys. Rev. B* **71**, 205214 (2005).
- [30] A. Togo, L. Chaput, I. Tanaka, and G. Hug, *Phys. Rev. B* **81**, 174301 (2010).
- [31] Z. He, X. Wang, W. Xu, Y. Zhou, Y. Sheng, Y. Rong, J. M. Smith, and J. H. Warner, *ACS Nano* **10**, 5847 (2016).
- [32] H. R. Gutiérrez, N. Perea-López, A. L. Elías, A. Berkdemir, B. Wang, R. Lv, F. López-Urías, V. H. Crespi, H. Terrones, and M. Terrones, *Nano Lett.* **13**, 3447 (2013).
- [33] J. S. Ross, S. F. Wu, H. Y. Yu, N. J. Ghimire, A. M. Jones, G. Aivazian, J. Q. Yan, D. G. Mandrus, D. Xiao, and W. Yao, *Nat. Commun.* **4**, 1474 (2013).
- [34] A. A. Mitioglu, P. Plochocka, J. N. Jadczak, W. Escoffier, G. L. J. A. Rikken, L. Kulyuk, and D. K. Maude, *Phys. Rev. B* **88**, 245403 (2013).
- [35] K. F. Mak, K. L. He, C. Lee, G. H. Lee, J. Hone, T. F. Heinz, and J. Shan, *Nat. Mater.* **12**, 207 (2013).
- [36] A. Splendiani, L. Sun, Y. Zhang, T. Li, J. Kim, C.-Y. Chim, G. Galli, and F. Wang, *Nano Lett.* **10**, 1271 (2010).
- [37] K. Chen, X. Wan, J. Wen, W. Xie, Z. Kang, X. Zeng, H. Chen, and J.-B. Xu, *ACS Nano* **9**, 9868 (2015).
- [38] See Supplemental Material at <http://link.aps.org/supplemental/10.1103/PhysRevB.98.245403> for details of the calculational Raman spectra and additional experimental data.
- [39] T. M. Nagaleekar and D. J. Late, *ACS Appl. Mater. Interfaces* **6**, 1158 (2014).
- [40] N. Peimyoo, J. Shang, W. Yang, Y. Wang, C. Cong, and T. Yu, *Nano Res.* **8**, 1210 (2014).
- [41] M. Balkanski, R. F. Wallis, and E. Haro, *Phys. Rev. B* **28**, 1928 (1983).

- [42] J. Judek, A. P. Gertych, K. Czerniak, and M. Zdrojek, *Phys. Chem. Chem. Phys.* **20**, 15486 (2018).
- [43] E. Schubert, T. Gessmann, and J. Kim, *Light Emitting Diodes* (Cambridge University Press, Cambridge, 2006).
- [44] C. Ji, Y. Zhang, T. Zhang, W. Liu, X. Zhang, H. Shen, Y. Wang, W. Gao, Y. Wang, J. Zhao, and W. W. Yu, *J. Phys. Chem. C* **119**, 13841 (2015).
- [45] T. Makino, K. Tamura, C. H. Chia, Y. Segawa, M. Kawasaki, A. Ohtomo, and H. Koinuma, *J. Appl. Phys.* **93**, 5929 (2003).
- [46] V. A. Fonoberov, K. A. Alim, A. A. Balandin, F. Xiu, and J. Liu, *Phys. Rev. B* **73**, 165317 (2006).
- [47] Y. P. Varshni, *Physica* **34**, 149 (1967).